AIAA Journal
Vol. 43, No. 9, September 2005

Numerical Simulation of Separation Control for Transitional Highly Loaded Low-Pressure Turbines

Donald P. Rizzetta* and Miguel R. Visbal†
U.S. Air Force Research Laboratory, Wright–Patterson Air Force Base, Ohio 45433-7512

The subsonic flow through highly loaded low-pressure turbines is simulated numerically using a high-order method. The configuration approximates cascade experiments that were conducted to investigate a reduction in turbine stage blade count, which can decrease both weight and mechanical complexity. At a nominal Reynolds number of 25×10^3 based upon axial chord and inlet conditions, massive separation occurs on the suction surface of each blade as a result of uncovered turning. Pulsed injection vortex generator jets were then used to help mitigate separation, thereby reducing wake losses. Computations were performed for both uncontrolled and controlled cases and reproduced the transitional flow occurring in the aft-blade and near-wake regions. The numerical method utilizes a centered compact finite difference scheme to represent spatial derivatives, which is used in conjunction with a low-pass Pade-type nondispersive filter operator to maintain stability. An implicit approximately factored time-marching algorithm is employed, and Newton-like subiterations are applied to achieve second-order temporal accuracy. Calculations were carried out on a massively parallel computing platform, using domain decomposition to distribute subzones on individual processors. A high-order overset grid approach preserved spatial accuracy in locally refined embedded regions. Features of the flowfields are elucidated, and simulations are compared with each other and with available experimental data. Relative to the uncontrolled case, it was found that pulsed injection maintained attached flow over an additional 15% of the blade chord, resulting in a 22% decrease of the wake total pressure loss coefficient.

Nomenclature

C_p = turbine blade time-mean surface-pressure coefficient, $2(\bar{p} - \bar{p}_i)/\rho_i \bar{q}_i^2$
c = turbine-blade axial chord
$\mathcal{D}$ = duty cycle expressed as a decimal fraction
d = nondimensional jet diameter
E_{k_z}, E_ω = turbulent kinetic energy wave number and frequency spectra
f = dimensional frequency
I, J, K = coordinate grid indices in the circumferential, blade normal, and spanwise directions
k_z = nondimensional spanwise wave number
l, n = nondimensional blade tangential and normal directions
P_t = nondimensional total pressure
p = nondimensional static pressure
q = nondimensional planar velocity magnitude, $\sqrt{(u^2 + v^2)}$ or $\sqrt{(v^2 + w^2)}$ for the jet
Re = chord inlet Reynolds number, $\rho_i \bar{q}_i Re_\infty / \mu_i$
Re_∞ = reference Reynolds number, $\rho_\infty q_\infty c / \mu_\infty$
s = nondimensional spanwise domain extent or nondimensional interjet spacing
t = nondimensional time based upon the reference velocity u_∞
t_p = nondimensional jet forcing period
u, v, w = nondimensional Cartesian velocity components in the x, y, z directions
x, y, z = nondimensional Cartesian coordinates in the streamwise, vertical, and spanwise directions
α = turbine-blade flow angle
$\Delta l, \Delta n, \Delta z$ = nondimensional mesh step sizes in blade tangential, normal, and spanwise directions
Δt = time-step size
ξ, η, ζ = body-fitted computational coordinates
ω = nondimensional frequency

Subscripts

i, o = inflow and outflow conditions
j = corresponding to vortex generator jet
ℓ = local freestream value
max, min = maximum and minimum values
∞ = dimensional reference value

Superscripts

$+$ = value given in law-of-the-wall units
$-$ = time-mean quantity
$'$ = rms fluctuating component

Introduction

ONE of the challenges arising in the use of uninhabited air vehicles (UAVs) for reconnaissance and combat missions is a loss of engine performance when such platforms operate in regimes of reduced atmospheric density. During high-altitude cruise, low-pressure turbines typically utilized by UAVs can encounter Reynolds numbers, based upon blade axial chord and inlet conditions, below 25×10^3. In such situations, boundary layers remain essentially laminar over a large portion of the turbine blades, even in the presence of elevated freestream turbulence levels. These laminar boundary layers are particularly susceptible to flow separation near the aft portion of a blade suction surface, resulting in a significant reduction in turbine efficiency, which can impose ceiling limitations for prolonged UAV operations.

A number of experimental studies[1–8] have been conducted in order to examine low-Reynolds-number effects on low-pressure turbines. These investigations have identified several factors contributing to performance degradation, which in addition to the Reynolds

---

Presented as Paper 2004-2204 at the AIAA 2nd Flow Control Conference, Portland, OR, 28 June–1 July 2004; received 21 July 2004; revision received 30 March 2005; accepted for publication 9 April 2005.

*Senior Research Aerospace Engineer, Computational Sciences Branch, Aeronautical Sciences Division. Associate Fellow AIAA.

†Technical Area Leader, Computational Sciences Branch, AFRL/VAAC. Associate Fellow AIAA.

number include freestream turbulence, pressure gradient, and curvature. It was found by Lake et al.[9] that boundary-layer separation, and the concurrent loss of efficiency, could be mitigated by modifying the turbine-blade geometry. Dimples were recessed into the blade suction surface in order to maintain the region of attached flow. Although such passive techniques have increased efficiency at low Reynolds numbers, they can also increase viscous losses at higher Reynolds numbers such as those that occur during takeoff, where unmodified blades perform satisfactorily. As an alternative, Bons et al.[10–12] and Sondergaard et al.[13] have implemented active flow control in the form of pulsed vortex generator jets. Extensive measurements verified that the jets dramatically reduced separation, resulting in decreased losses. Separation control in the form of a plasma actuator has also been demonstrated by Huang et al.[14]

More recent experiments by Sondergaard et al.[15] have explored the feasibility of increasing the blade spacing at constant chord for a linear low-pressure turbine cascade, thereby raising the per blade loading. For practical applications, a higher loading can reduce the turbine part count and stage weight. Increased blade spacing however is accompanied by increased boundary-layer separation on the suction surface of each blade as a result of uncovered turning and results in reduced efficiency and wake losses. Vortex generator jets were then employed to mitigate these losses by maintaining attached boundary-layer flow over a greater distance along the blade surface.

Several analytic efforts have focused on the critical issue of improved transition modeling for low-pressure turbine flows.[16–18] Numerical computations of these flows have traditionally been predicated on solution of the Reynolds-averaged Navier–Stokes (RANS) equations.[19–23] Although such endeavors have been moderately successful in predicting many of the overall features of low-pressure turbine flowfields, limitations and deficiencies of RANS turbulence models have precluded accurate calculation of the low-Reynolds-number effects on transition and separation. Moreover, it is unlikely that this approach will be adequate for the exploration of active flow control applications.

Advances in the speed and storage capacity of high-performance computing systems have now made it possible to perform very large-scale computations of representative turbine flow-fields. This has enabled Wu et al.[24] and Wu and Durbin[25] to study numerically both boundary-layer transition induced by periodically passing wakes upstream of a wall-bounded flow and the evolution of longitudinal vortices within a turbine passage. Direct numerical and large-eddy simulation have also emerged as viable means for the investigation of flows through low-pressure turbines[26–31] and for wing sections[32] and turbines with flow control.[33,34] The use of high-order numerical methods when applied to the low-Reynolds-number regime of interest offers the possibility of improved predictive capability. This is especially true for situations where RANS models fail and for the development of flow control strategies.

The purpose of the present work is to conduct numerical computations of the transitional flow through a highly loaded low-pressure turbine. The simulated geometry corresponds to the cascade experiments of Refs. 10–13 and 15, and calculations have been carried out at a chord inlet Reynolds number of approximately 25×10^3. Computations were performed for both uncontrolled and controlled cases, which can be contrasted with each other. Features of the flowfields are examined, the effect of vortex generator flow control is assessed, and comparison is made with available experimental data.

Governing Equations

The governing equations are taken as the unsteady three-dimensional compressible unfiltered Navier–Stokes equations. After introducing a curvilinear coordinate transformation to a body-fitted system, these are cast in the following nondimensional conservative form:

$$\frac{\partial \boldsymbol{Q}}{\partial t} + \frac{\partial}{\partial \xi}\left(\boldsymbol{F} - \frac{1}{Re_\infty}\boldsymbol{F}_v\right) + \frac{\partial}{\partial \eta}\left(\boldsymbol{G} - \frac{1}{Re_\infty}\boldsymbol{G}_v\right) + \frac{\partial}{\partial \zeta}\left(\boldsymbol{H} - \frac{1}{Re_\infty}\boldsymbol{H}_v\right) = 0 \tag{1}$$

Here, $\boldsymbol{Q}$ is the vector of dependent variables; $\boldsymbol{F}, \boldsymbol{G}, \boldsymbol{H}$ the inviscid flux vectors; and $\boldsymbol{F}_v$, $\boldsymbol{G}_v$, $\boldsymbol{H}_v$ the viscous flux vectors. A more detailed description of the governing equations can be found in Ref. 35 and is not reproduced here.

Numerical Method

Time-accurate solutions to Eq. (1) were obtained numerically by the implicit approximately factored finite difference algorithm of Beam and Warming[36] employing Newton-like subiterations,[37] which has evolved as an efficient tool for generating solutions to a wide variety of complex fluid flow problems. Efficiency was enhanced by solving the implicit portion of the factorized equations in diagonalized form,[38] and three subiterations per time step were applied for all computations.

Spatial derivatives were obtained by the compact difference scheme based upon the pentadiagonal system of Lele,[39] which is capable of attaining spectral-like resolution. For the present computations, a fourth-order tridiagonal subset of Lele's system was employed. It was used in conjunction with a sixth-order low-pass Pade-type nondispersive spatial filter developed by Gaitonde et al.,[40] which has been shown to be superior to the use of explicitly added artificial dissipation for maintaining both stability and accuracy on stretched curvilinear meshes.[41] The filter operator was applied to the solution vector sequentially in each of the three computational directions following each subiteration. Reference 35 provides more complete details of the numerical method.

The aforementioned features of the numerical algorithm are embodied in a parallel version of the time-accurate three-dimensional computer code FDL3DI,[42] which has proven to be reliable for steady and unsteady fluid flow problems, including the simulation of flows over delta wings with leading-edge vortices,[43–45] vortex breakdown,[44,45] direct numerical simulation (DNS) of transitional wall jets,[46] and synthetic jet actuators,[47] and DNS and large-eddy simulation of subsonic[29,48] and supersonic flowfields.[49–51]

Details of the Computations

The original experiments of Bons et al.[10–12] and Sondergaard et al.[13] consisted of a linear cascade of turbine blades having a span of 0.88 m and an axial chord of 0.18 m. The axial chord to spacing ratio (solidity, S) was 1.13, the inlet flow angle $\alpha_i = 35.0$ deg, and the design exit flow angle $\alpha_o = 60.0$ deg. Shown in Fig. 1 is a schematic representation of the turbine-blade shape, given by the Pratt and Whitney "PakB" research design, which is a Mach number scaled version of geometries typically used in highly loaded low-pressure turbines.[10–13,15] These experiments investigated the use of pulsed vortex generator jets to control the flow by mitigating the effects of separation on the blade suction surface. The jets were created by blowing air through holes that had been drilled in the blade surface at a pitch angle of 30 deg and a skew angle of 90 deg. Here, the pitch is defined as the angle the jet makes with the local surface, and the skew is the angle of the projection of the jet on the surface, relative to the local freestream direction.[12] The size of the drill used to develop the holes is commonly referred to as the jet diameter d, which was 0.001 m. Because of the orientation however, the jet-exit geometric shape is elliptic as seen in Fig. 1, and the jet-exit velocity vector has components only in the vertical y and spanwise z directions.

For the more highly loaded cascade investigation of Sondergaard et al.,[15] a series of experiments having increased interblade spacing

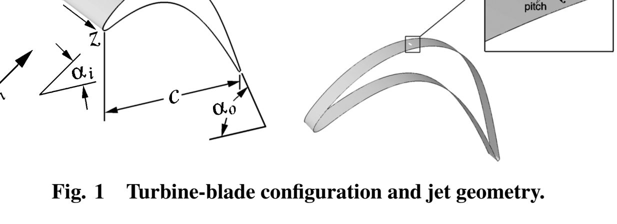

Fig. 1 Turbine-blade configuration and jet geometry.

Table 1 Geometric parameters

Reference	S	s	d	s/d	x_j
Bons et al.,[10–12] Sondergaard et al.[13]	1.13	5.56×10^{-2}	5.56×10^{-3}	10.0	0.63
Sondergaard et al.[15]	0.56–1.13	1.12×10^{-1}	1.12×10^{-2}	10.0	0.45
Present	0.75	5.56×10^{-2}	7.93×10^{-3}	7.0	0.37

Table 2 Computational mesh spacings in wall units

Grid	Points	Δt^+	$\Delta l^+_{\min}$	$\Delta l^+_{\max}$	$\Delta n^+_{\min}$	$\Delta z^+_{\min}$	$\Delta z^+_{\max}$
Coarse	5.3×10^6	0.04	1.14	49.48	0.30	6.50	6.50
Baseline	12.8×10^6	0.04	0.88	38.10	0.23	4.87	4.47
Flow control	17.9×10^6	0.05	0.58	46.86	0.30	0.91	2.76

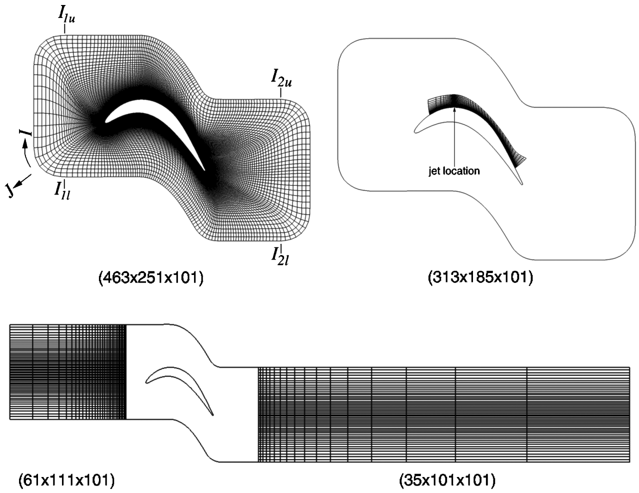

Fig. 2 Turbine computational meshes.

was conducted, thereby reducing the solidity. In this case the axial chord was 0.089 m, and the jet diameter was 0.01 m. A summary of nondimensional parameters for these experiments and the present computations can be found in Table 1.

Computational Meshes

To conserve computational resources, only a single turbine-blade passage was considered, and periodic conditions were enforced in the vertical direction y to represent a turbine stage flowfield. This situation is quite different than the experimental arrangement, which consisted of a small finite number of blades in a linear cascade. The computational domain surrounding the blade was described by a body-fitted mesh system, whose origin was located at the inboard leading edge of the blade (see Fig. 1). The mesh employed an O-grid topology, and was elliptically generated using automated software.[52] Figure 2 (upper left) indicates the baseline grid about the turbine blade for the uncontrolled case. Periodic conditions in the vertical direction were invoked along the boundaries $I_{1u} - I_{2u}$ and $I_{1l} - I_{2l}$.

To facilitate application of inflow and outflow conditions to the turbine-blade domain, overset grids were employed upstream and downstream of the blade region. These are also found in Fig. 2 (lower). The baseline grid employed 101 uniformly spaced grid points in the spanwise z direction, resulting in a total of approximately 12.8 million mesh points. Periodic spanwise conditions were invoked, utilizing a five-point overlap at the domain boundaries in the K direction. This overlap allowed application of periodic conditions while maintaining spatial accuracy. The extent of the spanwise domain was taken to be 0.2, which was described by a uniformly spaced mesh. A previous study of the domain extent for a similar low-pressure turbine by Rizzetta and Visbal[29] indicated that the value of 0.2 was adequate to allow the evolution of turbulent structures without artificially constraining their development.

The effect of grid resolution for the uncontrolled case was investigated by also constructing a coarse computational mesh. This grid had an identical computational structure and domain boundaries as that of the baseline mesh, but employed approximately 75% of the points in each coordinate direction. The blade domain consisted of $(348 \times 189 \times 75)$ points in (I, J, K) respectively.

To properly capture the correct fluid physics for the flow control case, the baseline grid was modified to enhance resolution in the jet and jet wake regions. This was done by removing grid points in the near wall region for $0.14 \leq x \leq 0.93$ and replacing them with an embedded refined mesh. The refined-mesh region appears in Fig. 2 (upper right), where only a fraction of the points are displayed. Within the refined-mesh region, a portion of the grid is cut out in the immediate vicinity of the jet exit. A series of overset grids was then employed to describe the elliptic jet geometry and the zones upstream, downstream, inboard, and outboard of the jet. These grids connect to each other and with the refined-mesh region.

The z extent for the flow control case was taken as the interjet spacing, and it was assumed that the flow was periodic in the spanwise direction, with the period specified as s (see Table 1). A nonuniform spanwise grid distribution was utilized, with grid-point clustering near the jet exit. Computational mesh spacings given in wall units for the three grid systems used in this investigation are presented in Table 2.

Temporal Considerations

Calculations for the uncontrolled case were obtained using a time step of $\Delta t = 0.00025$, where t is nondimensionalized by reference quantities. Based on inflow conditions, this corresponds to a time increment of approximately 0.00017 (see Table 2 for the time step in wall units). From an initial state, the flowfield was processed for 30,000 time steps to remove transients. Final results were then generated over a subsequent 42,000 steps, during which statistical information was collected. This duration represents 7.1 characteristic time units, based upon the inflow velocity.

Experimental investigations[10–13,15] have used several parameters to describe characteristics of unsteady vortex generating jets. The jet blowing ratio B is defined as

$$B = q_j / \bar{q}_l \tag{2}$$

where q_j is the jet-exit velocity magnitude and $\bar{q}_l$ is the local freestream velocity (see Ref. 11 for the definition of $\bar{q}_l$). The maximum value of the jet blowing ratio $B_{\max}$ was specified as 2.0. As a point of reference, typical film cooling holes for turbine applications are designed to operate at an approximate value of $B_{\max} = 2.0$ (Ref. 12). The experimental unsteady jet-exit velocity sequence consisted of a period of essentially constant blowing, followed by an interval of no blowing. The duty cycle is define as that portion of the total duration over which the jet is active and was 50% for the present case. A nondimensional frequency $\mathcal{F}$ as defined in Refs. 10–13 was used to quantify the forcing period where

$$\mathcal{F} = \frac{0.41 c f_j}{u_\infty \bar{q}_i} \tag{3}$$

A value of $\mathcal{F} = 3.1$ was used in the computations, which was the same as that of some experiments.[10–12]

An experimental[12] time history of one blowing cycle obtained by hot-wire measurement appears in Fig. 3. For the computations, a simple piecewise continuous function was used to approximate the experimental result. The 50% duty cycle is apparent in the figure. For the flow control computation, a time step of $\Delta t = 0.00019$ ($\Delta t = 0.00014$ based upon inflow conditions) was employed, which corresponds to 1000 steps per period t_p of the cycle indicated in Fig. 3. The computational flowfield for the flow control case was initialized from the uncontrolled result and temporally evolved for 21,000 time steps. Statistical information was then collected for 63,000 steps, representing 8.8 characteristic time units, based upon the inflow velocity.

For the flow control case, the piecewise continuous temporal variation of the jet blowing ratio B presented in Fig. 3 was used to specify

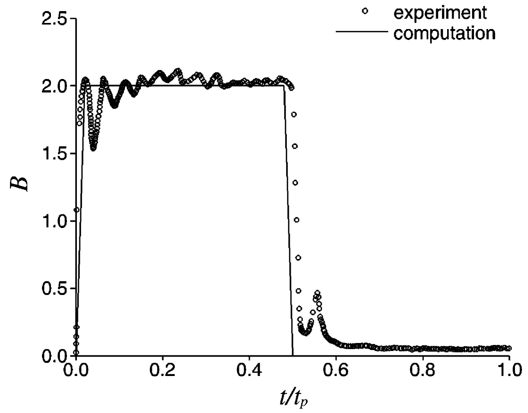

Fig. 3 Jet blowing ratio time history.

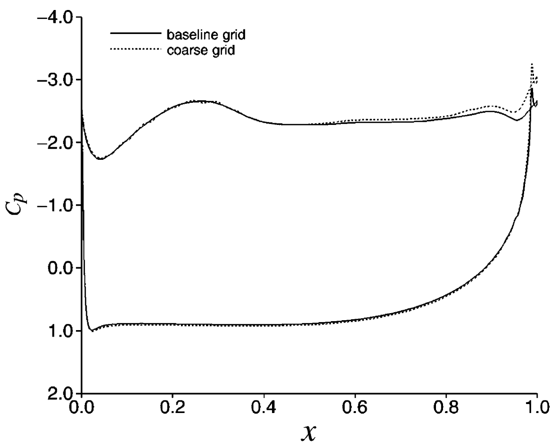

Fig. 4 Time-mean spanwise-averaged surface-pressure coefficient distributions for the baseline and coarse grids.

the instantaneous exit velocity at the center of the vortex generator jet. In terms of the reference condition, the maximum value of the jet-exit velocity corresponding to $B_{\max} = 2.0$ was $q_{j\max} = 2.52$. A flat-top jet profile was assumed, with a linear variation from no slip at the edges of the jet, to the constant center value. The jet was assumed to be isothermal, and the exit pressure was obtained from the inviscid normal momentum equation, which was solved with second-order temporal and fourth-order spatial accuracy.

Boundary Conditions

A complete description of the boundary conditions for all of the simulations is given in Ref. 35.

Results

Effect of Grid Resolution

To assess accuracy of the computations, comparisons for a number of quantities were made between results obtained on the coarse and baseline meshes, respectively. These quantities have been temporally averaged, as well as averaged across the span, owing to the homogeneous property in the spanwise direction. Time-mean surface-pressure coefficient distributions for these cases are displayed in Fig. 4. Apart from small differences at the trailing edge, the distributions are virtually identical. Time-mean profiles of velocity magnitude, along a normal to the blade surface at several streamwise locations, are found in Fig. 5. In the figure, the normal distance n has been nondimensionalized by the turbine blade chord, and the velocity magnitude has been normalized by the inflow velocity $\bar{q}_i$. Only slight disparities between the two solutions are apparent at the downstream stations, where the massively separated flow is highly unsteady. Shown in Fig. 6 are corresponding profiles of the rms velocity magnitude fluctuations. Again, differences are observed in the downstream locations.

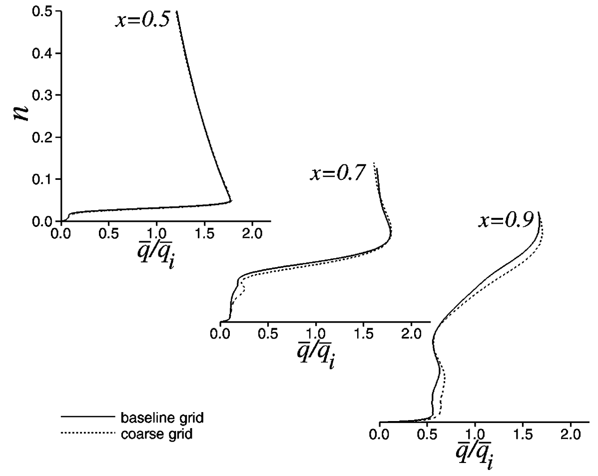

Fig. 5 Time-mean spanwise-averaged velocity magnitude profiles for the baseline and coarse grids.

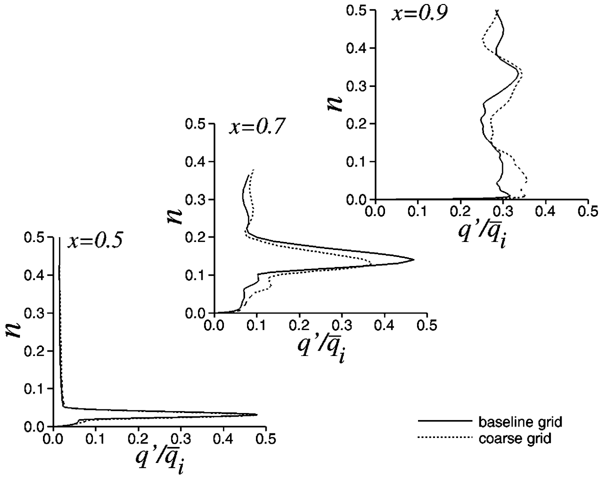

Fig. 6 Time-mean spanwise-averaged fluctuating velocity magnitude profiles for the baseline and coarse grids.

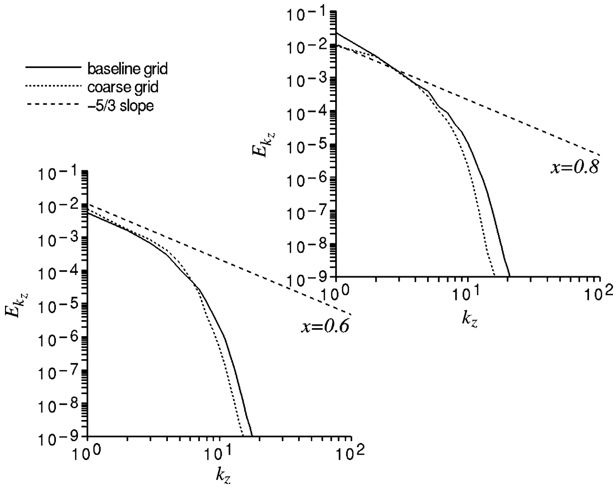

Fig. 7 Time-mean turbulent-kinetic-energy spanwise wave-number spectra for the baseline and coarse grids.

Resolution in the spanwise direction was examined by observing the turbulent kinetic energy spatial wave-number spectrum. This can be seen at two locations in Fig. 7. Spanwise spectra were generated at each time step, and these were then temporally averaged to construct results appearing in the figure. At each station, the spectra were taken at a normal distance from the blade surface of $n = 0.03$, which was approximately one-half of a boundary-layer thickness of the time-mean velocity profile upstream of separation. Because the flow is transitional, most of the energy is contained at low wave numbers, corresponding to large-scale structures. Subsequently, there is not a pronounced region in wave number that lies in the inertial range, where the slope of E_{k_z} is $-\frac{5}{3}$. The figure indicates that even on the coarse computational mesh the turbulent kinetic energy is reasonably well resolved.

Time-Mean Flowfields

Time-mean surface pressure coefficient distributions for the baseline and flow control computations are compared in Fig. 8. The baseline distribution is the same as that presented in Fig. 4. Because of the jet orientation, homogeneity could not be assumed in the z direction for the flow control case. Consequently, spanwise averaging was not employed for that result, and the distribution in the figure was obtained at a z location, which was midway between two jets (i.e., on the periodic boundary). The large plateau region in the baseline distribution, which is characteristic of massive separation, has been reduced by flow control. The effect of flow control is to decrease the pressure on the upstream portion of the suction surface, while increasing it downstream, relative to the baseline case. This is caused by reduced blockage and a subsequent increase of the flow velocity through the blade passage.

Time-mean profiles of velocity magnitude are presented in Figs. 9 and 10. Although no experimental data that match the exact geometrical parameters and flow conditions of the computations are available, it is useful to compare numerical results with the measurements of Sondergaard et al.,[15] which were taken for an investigation of a similar situation. A number of significant differences exist, however, between the computational and experimental arrangements, so that this comparison can only be considered to be qualitative. First, the experimental data were collected within a linear cascade with a limited number of blades, whereas the computatious correspond to the periodic situation in a single turbine stage. Additionally, tail boards were attached at the trailing edge of the first and last blades in the cascade and extended a considerable distance into the wake. At low Reynolds numbers, this arrangement was found to be significant in previous computations.[29,33] Second, the experiments were conducted at a nominal Reynolds number of 5×10^4, whereas the calculations were performed for $Re \approx 25 \times 10^3$. A low Reynolds number was employed in the calculations as it would result in massive separation and because it more nearly corresponded to high-altitude cruise conditions for UAVs. As noted in Table 1, both the inter-jet spacing and jet diameter of the experiment are larger than those of the computations.

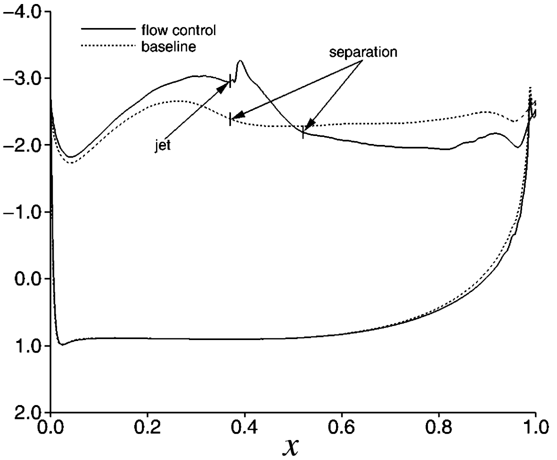

Fig. 8 Time-mean surface-pressure coefficient distributions for the baseline and flow control cases.

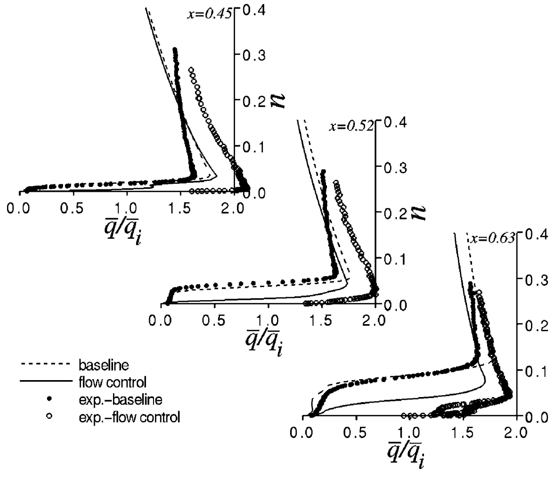

Fig. 9 Time-mean velocity magnitude profiles for the baseline and flow control cases.

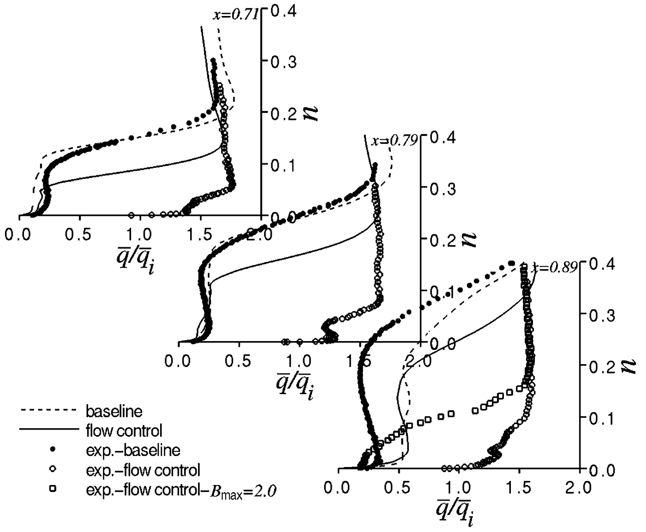

Fig. 10 Time-mean velocity magnitude profiles for the baseline and flow control cases.

It was suggested in Ref. 15 that flow control jets should be located very near to the time-mean separation point. For the baseline case, this was found to occur at $x = 0.37$, which was then specified as the jet position x_j. Because of the higher Reynolds number, the separation point and subsequent jet location of the experiment were at $x = 0.45$. In addition, the maximum value of the jet blowing ratio was $B_{\max} = 4.5$ for the experiment, whereas that of the computation was $B_{\max} = 2.0$. The experimental blowing ratio and jet diameter led to a jet blowing coefficient of $c_\mu = 2.43 \times 10^{-2}$, which was orders of magnitude larger than that of the calculation where $c_\mu = 9.88 \times 10^{-5}$. Here the jet blowing coefficient is defined as

$$c_\mu = \mathcal{D}\left[(\pi/4)d^2 B_{\max}^2\right] \quad (4)$$

Furthermore, evenly spaced jets were distributed along the span of only the center blade in the experimental cascade. No flow control was imposed on blades above or below the central blade. This was unlike the computational arrangement, which employed periodic boundary conditions to simulate flow control on all blades in a single-stage configuration. Finally, a major difference between the computations and experiments is that only results with steady blowing used to generate flow control were available for the experimental data.

As in previous figures, n is the nondimensional distance normal to the blade suction surface, $\bar{q}$ has been normalized by the time-mean inflow velocity $\bar{q}_i$, and baseline results have been spanwise averaged. No spanwise averaging was applied for flow control profiles, which correspond to a spanwise position between jets, in accordance with the experimental location at which data were taken. For the baseline profiles, differences between the computational and experimental results appear to be consistent with the differences in the respective Reynolds numbers. When flow control is applied, fullness of the time-mean profiles is increased as a result of enhanced mixing. Although control is less effective for the computation than for the experiment because of the disparity in the jet momentum coefficient and Reynolds number, the comparison is qualitatively favorable. Numerically, it can be seen from Fig. 9 that attached flow was maintain up to $x = 0.52$. While the time-mean separation point varied across the span, its averaged value was $x \approx 0.52$. At $x = 0.89$ there is an additional experimental result for $B_{\max} = 2.0$. The difference in experimental profiles for $B_{\max} = 2.0$ and 4.5 indicate the considerable sensitivity to jet blowing parameters.

Spanwise turbulent kinetic energy wave-number spectra are provided in Fig. 11. These spectra were generated along lines in the z direction at a distance of $n = 0.03$ from the blade surface and constructed by the technique already described. Although the kinetic energy amplitude of the flow control case is somewhat higher than that of the baseline case at $x = 0.6$, it is considerably lower at $x = 0.8$. The absence of an inertial range in wave number is once more noted.

Time-mean contours of the streamwise component of velocity u appear in Fig. 12a. For the baseline case, the contours have also been spanwise averaged. The contours for the flow control result were taken at the spanwise location corresponding to the center of the jet. Near the jet location indicated in the flow control contours, a greater region of attached flow, relative to the baseline case, can be observed. The wake region near the trailing edge is also noticeable reduced by flow control. This reduction can be quantified by the integrated wake pressure loss coefficient C_w, defined as[15]

$$C_w = S \int \left(\frac{P_{\mathrm{ti}} - \bar{P}_{\mathrm{to}}}{P_{\mathrm{ti}} - \bar{p}_i} \right) \mathrm{d}y \tag{5}$$

where the integration takes place across the wake profile between the periodic boundaries in the vertical direction. It was found that $C_w = 1.10$ for the baseline calculation and $C_w = 0.86$ for the flow control case, resulting in a 22% decrease in the total pressure wake loss when pulsed injection is employed.

Figures 12b and 12c also display time-mean contours of the spanwise component of vorticity. The contours for the baseline case have been spanwise averaged. The upper segment of each frame gives contours on the blade surface, for the area outlined by the rectangular box. Contours for the lower frame of the flow control case were taken at a plane lying between jets. Dark contours at the upper-right portion of the figure surrounding the jet signify the region of attached flow. The zones highlighted by rectangular boxes demonstrate that use of flow control has kept the turbine-blade shear layer confined to the surface for a greater streamwise extent.

Unsteady Features of the Flowfields

Profiles of the rms fluctuating velocity magnitude, for both the baseline and flow control cases, are shown at several steamwise locations in Fig. 13. Here again, the baseline profiles have been spanwise averaged, while the flow control results are taken at a z location between the jets. At this position in the span, the effect of control is to reduce the magnitude of the fluctuations. Turbulent kinetic energy frequency spectra at these same locations are seen in Fig. 14. The designation "tev" signifies the shedding frequency of the trailing-edge vortex. In the baseline spectra at $x = 0.6$, there is a broad amplification of energy near $\omega \approx 5.79$ that is associated with the unsteady shear layer. At this same x location, the flow control spectra display harmonics corresponding to the jet pulsing frequency, in addition to the broad amplification. The first harmonic of the jet forcing occurs at $\omega = 7.14$. Note that the trailing-edge vortex shedding frequency has been reduced from $\omega = 0.71$ in the baseline case to $\omega = 0.34$ with flow control. Downstream at $x = 0.8$, the location at which the spectra were taken lies near the blade surface within a massively separated region. Consequently, no amplification of turbulent kinetic energy occurs. This location is also far enough removed from the pulsing jet to be effectively out of its influence.

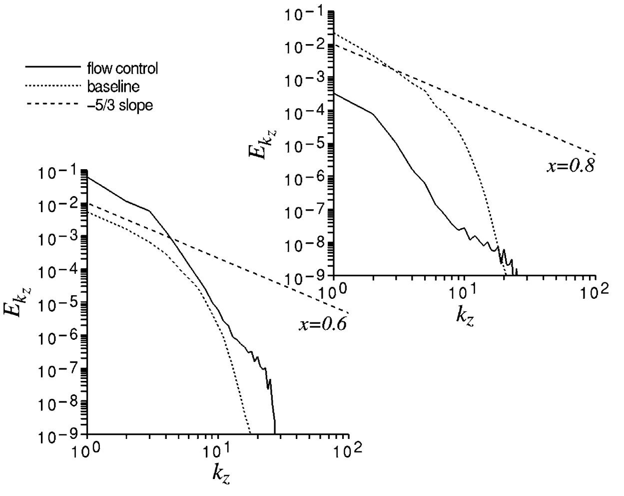

Fig. 11 Time-mean turbulent-kinetic-energy spanwise wave-number spectra for the baseline and flow control cases.

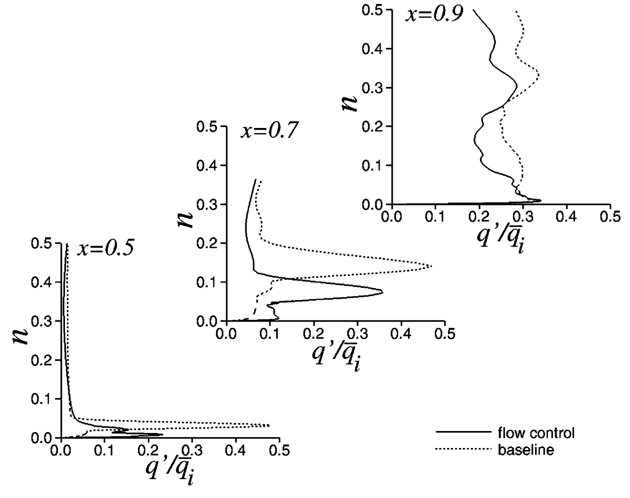

Fig. 13 Time-mean fluctuating velocity magnitude profiles for the baseline and flow control cases.

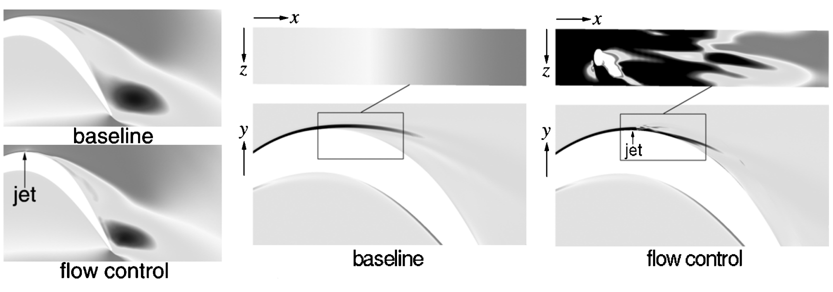

a) b) c)

Fig. 12 Time-mean planar contours of u velocity and z vorticity.

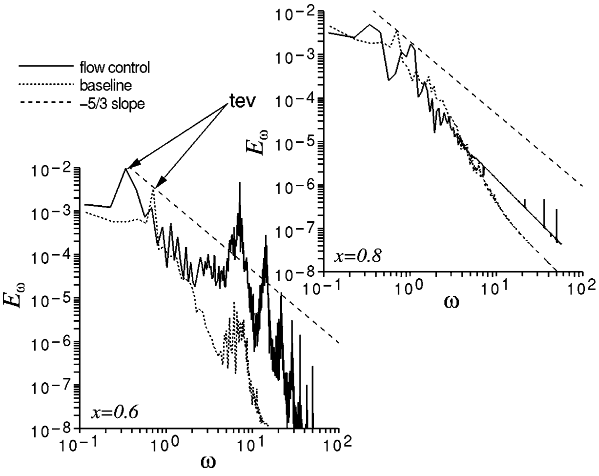

Fig. 14 Turbulent-kinetic-energy frequency spectra for the baseline and flow control cases.

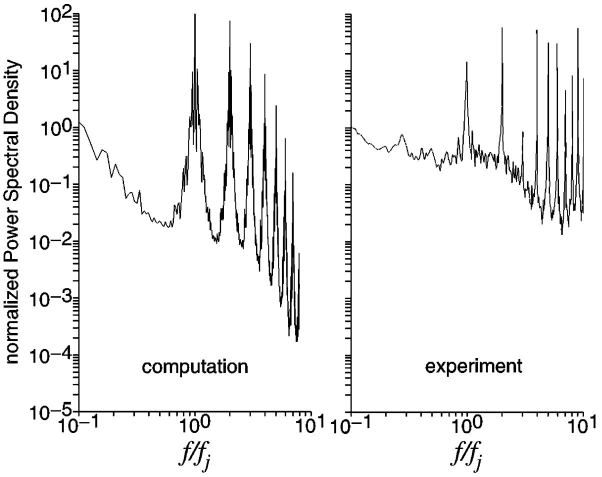

Fig. 15 Power spectral density frequency spectra for the flow control case.

The power spectral density from the flow control computation is compared to the experimental data of Bons et al.[11] in Fig. 15. Although the Reynolds number of both the simulation and the experiment is 25×10^3, the interblade spacings are different (see Table 1). The experimental data were taken downstream of the jet where $x - x_j = 0.18$, at a distance from the blade surface approximately equal to one boundary-layer thickness, and the maximum jet blowing ratio was $B_{\max} = 0.2$. Computational information was collected at $x - x_j = 0.13$ and n equal to one-half a boundary-layer thickness with $B_{\max} = 2.0$. The frequency in the figure has been nondimensionalized by the jet pulsing frequency f_j. And because of differences between the simulation and the experiment, the power spectral density has been normalized by its value at $f/f_j = 0.1$. Qualitative agreement between the two spectra is evident in the figure. It is observed that peaks in the spectra occur at each harmonic of the forcing frequency. This is attributable to the frequency content of the pulsed jet velocity, which was demonstrated previously.[35] In Ref. 35, the time history of the jet blowing ratio B was generated, and the frequency spectrum for B was then extracted from the time history. The resulting spectrum for B was found to be quite similar to Fig. 15 (see Ref. 35, Fig. 22). Time histories of the turbulent kinetic energy for the flow control also appear in Ref. 35.

To elucidate features of the unsteady turbine blade flowfield, a series of planar contours for both the baseline and flow control cases is presented at four distinct instances in time. The flowfield is characterized by a shear layer emanating from the detached boundary layer near the blade midchord, which evolves into a massively separated region. In addition, a vortex forms at the trailing edge, rolls up in a counterclockwise direction (in the view of a figure), and is shed into the wake. The time sequence $t = t_1, t_2, t_3, t_4$ represents one cycle of this shedding frequency, divided into equally spaced intervals. Vortex shedding also occurs from the massively separated region upstream of the trailing edge. In this case however, the shed vortices are not as discrete, and the shedding is not as regular as that at the trailing edge. Instantaneous contours of the streamwise velocity component u are seen in Figs. 16 and 17. Baseline contours were taken at the blade midspan, whereas those of the flow control case were situated between the control jets. The shear layer and massively separated region are visible in the figures. A careful inspection of Fig. 17 reveals a greater distance over which the boundary layer remains attached and less vertical extent of the separated region for the flow control case. Corresponding contours of the spanwise component of vorticity are provided in Figs. 18 and 19. In this presentation, the vortical structures can be clearly discerned. The more massive separation in the baseline case gives rise to fine-scale features caused by instabilities in the spanwise direction, which can be identified in Fig. 18. These are absent in Fig. 19, where effects of separation have been mitigated by pulsed injection.

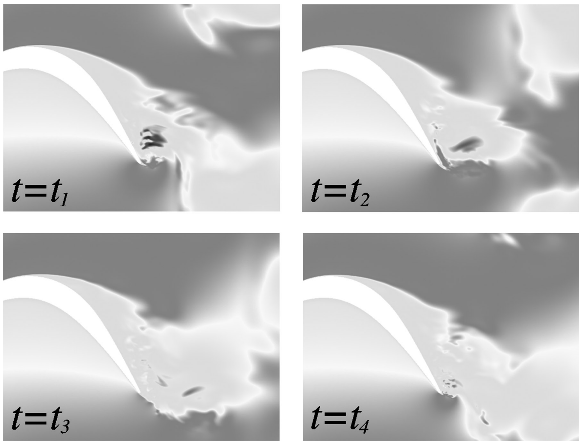

Fig. 16 Instantaneous planar contours of u velocity for the baseline case.

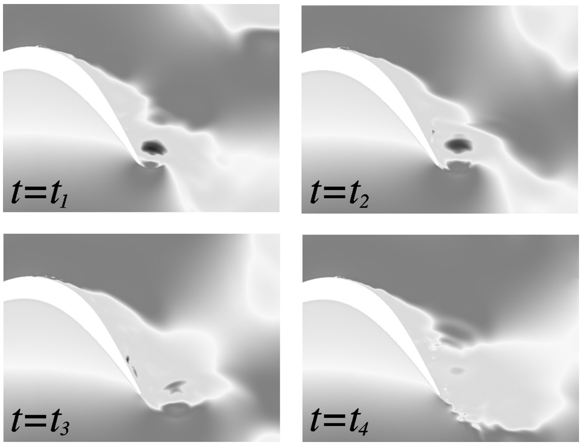

Fig. 17 Instantaneous planar contours of u velocity for the flow control case.

A three-dimensional representation of the separated turbine blade flowfield is found in Figs. 20 and 21 in terms of instantaneous isosurfaces of vorticity magnitude at the four discrete instances in time. For the view observed in Fig. 21, the spanwise coordinate z has been artificially stretched to more clearly reveal details of the flow. The value of the isosurfaces corresponds approximately to that at the edge of the boundary layer in the upstream attached flow. A more complex flowfield is again indicated in the baseline result. Figure 20 illustrates the transitional nature of the turbine blade flow, whereby fine-scale structures evolve within the chaotic, massively separated region. This is unlike the traditional evolution of turbulence for wall-bounded flows.

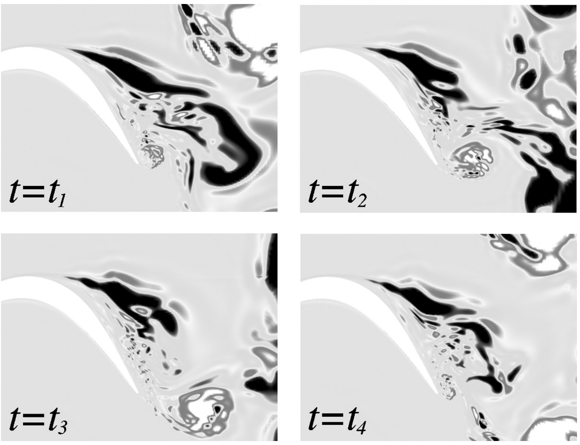

Fig. 18 Instantaneous planar contours of the spanwise component of vorticity for the baseline case.

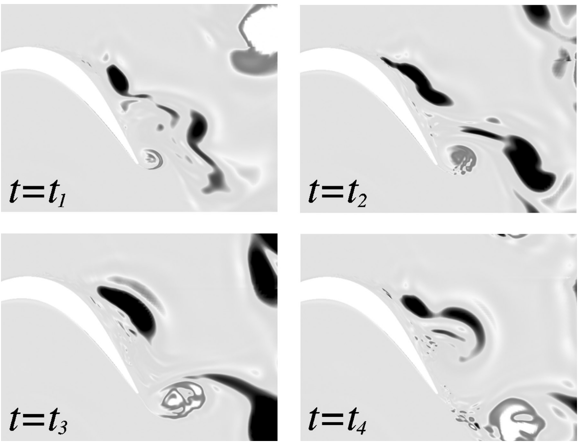

Fig. 19 Instantaneous planar contours of the spanwise component of vorticity for the flow control case.

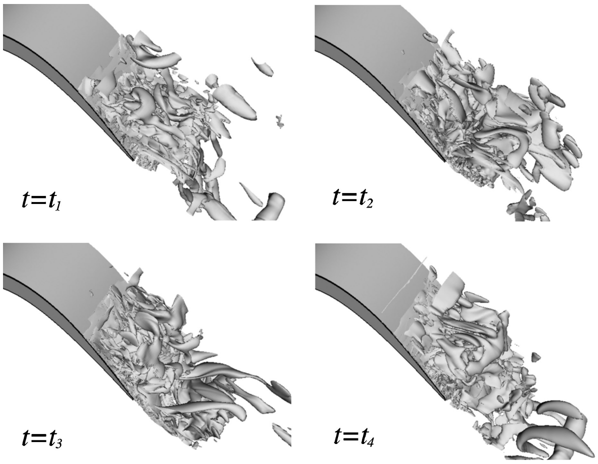

Fig. 20 Instantaneous isosurfaces of vorticity magnitude for the baseline case.

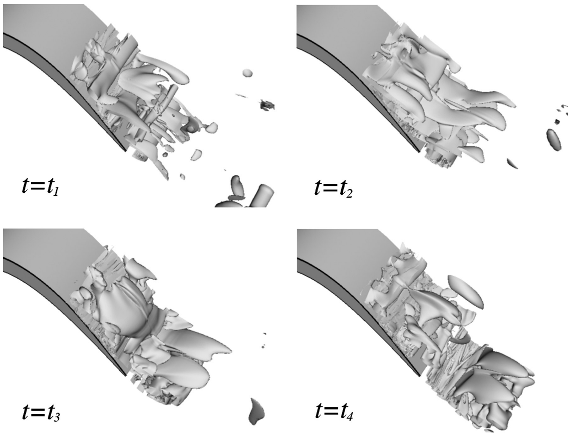

Fig. 21 Instantaneous isosurfaces of vorticity magnitude for the flow control case.

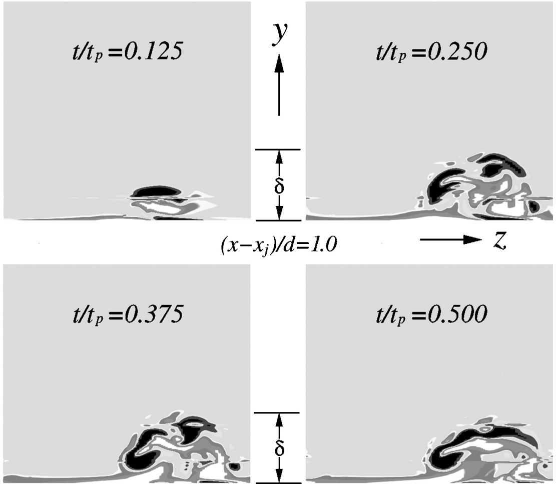

Fig. 22 Instantaneous planar contours of the streamwise component of vorticity for the flow control case.

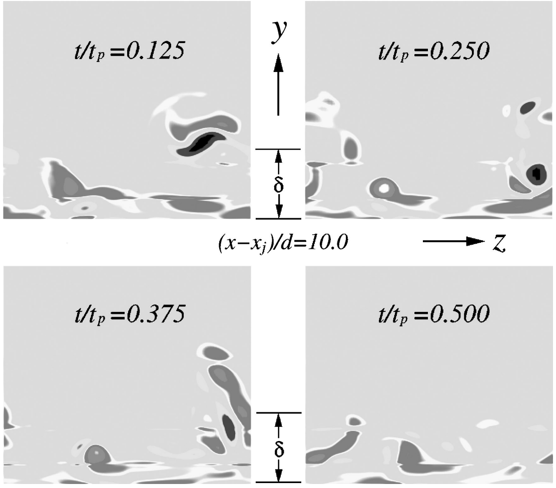

Fig. 23 Instantaneous planar contours of the streamwise component of vorticity for the flow control case.

Features of the near-jet flowfield are evidenced by instantaneous contours of the streamwise component of vorticity displayed in Figs. 22 and 23. The view in these figures is at a constant x location, looking downstream toward the blade trailing edge. Streamwise positions are at distances of one and 10 jet diameters downstream from the point of injection, respectively. The series of frames in each figure represent discrete instances in time within one period of the jet blowing cycle displayed in Fig. 3. Dark contours correspond to regions of negative vorticity with counterclockwise rotation, while positive vorticity and clockwise rotation is associated with lighter contours. The height of the attached boundary layer upstream of injection appears as δ. When $t/t_p = 0.125$, the jet has just attained its maximum velocity. Vorticity was generated through entrainment of surrounding fluid and can be seen emerging in Fig. 22. Because of the low pitch angle of the jet, the areas of vorticity with opposite sign are visible as flat horizontal bands. For $t/t_p > 0.125$, flow at the near-jet location $(x - x_j)/d = 1.0$ has attained a somewhat equilibrium condition. Injection has penetrated to the height of the boundary layer, which is essential to controlling the flow. At $t/t_p = 0.500$, pulsing of the jet terminates (see Fig. 3). Features seen at the downstream station $(x - x_j)/d = 10.0$ in Fig. 23 were produced by the pulse prior to that shown in Fig. 22, which have now convected downstream. Although no persistent, coherent vortical structures can be identified in these figures, considerable mixing is clearly evident. This is attributable to the complex nature of the unsteady injection into an adverse pressure gradient flow.

Summary

Direct simulation was used to describe the subsonic flow through a highly loaded low-pressure turbine at a nominal Reynolds number of 25×10^3. Unsteady computations for baseline and pulsed injection flow control flowfields were carried out using a high-order numerical method. An overset grid technique was employed for modeling the region surrounding the jet, and high-order interpolation was employed to maintain spatial accuracy. A grid mesh-size study of the baseline case was performed and indicated adequacy of the resolution. A comprehensive comparison between the baseline and flow control cases was then conducted.

Although the computational flowfields differed considerably from those of similar experimental investigations, reasonable agreement was found between numerical results and measurements of time-mean velocity magnitude profiles. Turbulent-kinetic-energy spatial wave-number spectra indicated the transitional nature of the flowfields. For the flow control case, the energy temporal frequency spectrum was dominated by the pulsed injection in the area near to the control jet. This effect diminished farther downstream. The baseline case was characterized by vortex shedding at the trailing edge and massive separation, which gave rise to a complex and chaotic region containing fine-scale fluid structures. Because flow control reduced the size and strength of the trailing-edge vortex, its shedding frequency was reduced by 50%. Use of a high-order numerical method was critical in capturing the physical features correctly.

As was found experimentally, the numerically simulated pulsed injection flow control jets were able to mitigate effects of the extensive separation that occurred at low Reynolds number, through enhanced mixing of the near-wall flow. This maintain attached flow along the blade surface for an additional 15% of the chord, which then resulted in a 22% reduction of the integrated wake total pressure loss coefficient. This gain in performance might be improved through the use of a larger jet momentum coefficient, by increasing either the jet diameter or the blowing ratio. It is also believed that additional jets spaced at intervals along the blade surface might be useful for maintaining the quality of the flow and level of performance over a wider range of conditions. In this regard, numerical simulation can be instrumental for exploring this and other flow control strategies.

Acknowledgments

The work presented here was sponsored by the U. S. Air Force Office of Scientific Research under Task 2307N61A and was monitored by T. Beutner. Computational resources were supported in part by a grant of supercomputer time from the U. S. Department of Defense Major Shared Resource Centers at Stennis Space Center, Mississippi, and Wright–Patterson Air Force Base, Ohio. The authors are grateful to R. Sondergaard for supplying experimental results. They also acknowledge S. E. Sherer for assistance with the high-order interpolation and P. E. Morgan for a number of helpful discussions.

References

[1] Halstead, D. E., Wisler, D. C., Okiishi, T. H., Walker, G. J., Hodson, H. P., and Shin, H. W., "Boundary Layer Development in Axial Compressors and Turbines Part 1 of 4: Composite Picture," American Society of Mechanical Engineers, Paper 95-GT-461, June 1995.

[2] Halstead, D. E., Wisler, D. C., Okiishi, T. H., Walker, G. J., Hodson, H. P., and Shin, H. W., "Boundary Layer Development in Axial Compressors and Turbines Part 3 of 4: LP Turbines," American Society of Mechanical Engineers, Paper 95-GT-463, June 1995.

[3] Simon, T. W., and Volino, R. J., "Separating and Separated Boundary Layers," Wright Lab., Technical Rept. WL-TR-96-2092, Wright–Patterson AFB, OH, Feb. 1996.

[4] Baughn, J. W., Butler, R. J., Byerley, A. R., and Rivir, R. B., "An Experimental Investigation of Heat Transfer, Transition and Separation on Turbine Blades at Low Reynolds Number and High Turbulence Intensity," Wright Lab., Technical Rept. WL-TR-96-2093, Wright–Patterson AFB, OH, July 1996.

[5] Murawski, C. G., Simon, T. W., Volino, R. J., and Vafai, K., "Experimental Study of the Unsteady Aerodynamics in a Linear Cascade with Low Reynolds Number Low Pressure Turbine Blades," American Society of Mechanical Engineers, Paper 97-GT-95, June 1997.

[6] Qui, S., and Simon, T. W., "An Experimental Investigation of Transition as Applied to Low Pressure Turbine Suction Surface Flows," American Society of Mechanical Engineers, Paper 97-GT-455, June 1997.

[7] Welsh, S. T., Barlow, D. N., Butler, R. J., Van Treuren, K. W., Byerley, A. R., Baughn, J. W., and Rivir, R. B., "Effects of Passive and Active Air-Jet Turbulence on Turbine Blade Heat Transfer," American Society of Mechanical Engineers, Paper 97-GT-131, June 1997.

[8] Murawski, C. G., and Vafai, K., "Effect of Variable Axial Chord on a Low-Pressure Turbine Blade," *Journal of Propulsion and Power*, Vol. 15, No. 5, 1999, pp. 667–674.

[9] Lake, J. P., King, P. I., and Rivir, R. B., "Reduction of Separation Losses on a Turbine Blade with Low Reynolds Number," AIAA Paper 99-0242, Jan. 1999.

[10] Bons, J. P., Sondergaard, R., and Rivir, R. B., "Control of Low-Pressure Turbine Separation Using Vortex Generator Jets," AIAA Paper 99-0367, Jan. 1999.

[11] Bons, J. P., Sondergaard, R., and Rivir, R. B., "Turbine Separation Control Using Pulsed Vortex Generator Jets," *Journal of Turbomachinery*, Vol. 123, No. 2, 2001, pp. 198–206.

[12] Bons, J. P., Sondergaard, R., and Rivir, R. B., "The Fluid Dynamics of LPT Blade Separation Control Using Pulsed Jets," *Journal of Turbomachinery*, Vol. 124, No. 1, 2002, pp. 77–85.

[13] Sondergaard, R., Rivir, R. B., and Bons, J. P., "Control of Low-Pressure Turbine Separation Using Vortex Generator Jets," *Journal of Propulsion and Power*, Vol. 18, No. 4, 2002, pp. 889–895.

[14] Huang, J., Corke, T. C., and Thomas, F. O., "Plasma Actuators for Separation Control of Low Pressure Turbine Blades," AIAA Paper 2003-1027, Jan. 2003.

[15] Sondergaard, R., Bons, J. P., Sucher, M., and Rivir, R. B., "Reducing Low-Pressure Turbine Stage Blade Count Using Vortex Generator Jet Separation Control," American Society of Mechanical Engineers, Paper GT-2002-30602, June 2002.

[16] Mayle, R. E., "The Role of Laminar-Turbulent Transition in Gas Turbine Engines," American Society of Mechanical Engineers, Paper 91-GT-261, June 1991.

[17] Gostelow, J. P., Blunden, A. R., and Walker, G. J., "Effects of Free-Stream Turbulence and Adverse Pressure Gradients on Boundary Layer Transition," *Journal of Turbomachinery*, Vol. 116, No. 3, 1994, pp. 392–404.

[18] Boyle, R. J., and Simon, F. F., "Mach Number Effects on Turbine Blade Transition Length Prediction," American Society of Mechanical Engineers, Paper 98-GT-367, June 1998.

[19] Eulitz, F., and Engel, K., "Numerical Investigation of Wake Interaction in a Low Pressure Turbine," American Society of Mechanical Engineers, Paper 98-GT-563, June 1998.

[20] Choi, C. H., and Yoo, J. Y., "Cascade Flow Calculations Using the k–ω Turbulence Model with Explicit-Implicit Solver," *AIAA Journal*, Vol. 35, No. 9, 1998, pp. 1551, 1552.

[21] Chernobrovkin, A., and Lakshminarayana, B., "Turbulence Modeling and Computation of Viscous Transitional Flows for Low Pressure Turbines," *Journal of Fluids Engineering*, Vol. 121, No. 4, 1999, pp. 824–833.

[22] Dorney, D. J., Ashpis, D. E., Halstead, D. E., and Wisler, D. C., "Study of Boundary-Layer Development in a Two-Stage Low-Pressure Turbine," *Journal of Propulsion and Power*, Vol. 16, No. 1, 2000, pp. 160–163.

[23] Suzen, Y. B., Huang, P. G., Hultgren, L. S., and Ashpis, D. E., "Predictions of Separated and Transitional Boundary Layers Under Low-Pressure Turbine Airfoil Conditions Using an Intermittency Transport Equation," AIAA Paper 2001-0446, Jan. 2001.

[24] Wu, X., Jacobs, R. G., Hunt, J. C. R., and Durbin, P. A., "Simulation of Boundary Layer Transition Induced by Periodically Passing Wakes," *Journal of Fluid Mechanics*, Vol. 398, Nov. 1999, pp. 109–153.

[25] Wu, X., and Durbin, P. A., "Evidence of Longitudinal Vortices Evolved from Distorted Wakes in a Turbine Passage," *Journal of Fluid Mechanics*, Vol. 446, Nov. 2001, pp. 199–228.

[26] Raverdy, B., Mary, I., Sagaut, P., and Liamis, N., "Large-Eddy Simulation of the Flow Around a Low Pressure Turbine Blade," *Direct and Large-Eddy Simulation IV, ERCOFTAC Series*, Vol. 8, edited by B. J. Guerts, R. Friedrich, and O. Metais, Kluwer Academic, Dordrecht, The Netherlands, 2001, pp. 381–388.

[27] Raverdy, B., Mary, I., Sagaut, P., and Liamis, N., "High-Resolution Large-Eddy Simulation of Flow Around Low Pressure Turbine Blade," *AIAA Journal*, Vol. 41, No. 3, 2003, pp. 390–397.

[28] Mittal, R., Venkatasubramanian, S., and Najjar, F. M., "Large-Eddy Simulation of Flow Through a Low-Pressure Turbine Cascade," AIAA Paper 2001-2560, June 2001.

[29] Rizzetta, D. P., and Visbal, M. R., "Numerical Investigation of Transitional Flow Through a Low-Pressure Turbine Cascade," AIAA Paper 2003-3587, June 2003.

[30] Wissink, J. G., "DNS of Separating, Low-Reynolds Number Flow in a Turbine Cascade with Incoming Wakes," *International Journal of Heat and Fluid Flow*, Vol. 24, No. 4, 2003, pp. 626–635.

[31] Kalitzin, G., Wu, X., and Durbin, P. A., "DNS of Fully Turbulent Flow in a LPT Passage," *International Journal of Heat and Fluid Flow*, Vol. 24, No. 4, 2003, pp. 636–644.

[32] Jiang, L., and Liu, C., "Direct Numerical Simulation for Flow Separation Control with Pulsed Jets," AIAA Paper 2003-0611, Jan. 2003.

[33] Postl, D., Gross, A., and Fasel, H. F., "Numerical Investigation of Low-Pressure Turbine Blade Separation Control," AIAA Paper 2003-0614, Jan. 2003.

[34] Postl, D., Gross, A., and Fasel, H. F., "Numerical Investigation of Active Flow Control for Low-Pressure Turbine Blade Separation," AIAA Paper 2004-750, Jan. 2004.

[35] Rizzetta, D. P., and Visbal, M. R., "Numerical Simulation of Separation Control for a Highly-Loaded Low-Pressure Turbine," AIAA Paper 2004-2204, June–July 2004.

[36] Beam, R., and Warming, R., "An Implicit Factored Scheme for the Compressible Navier–Stokes Equations," *AIAA Journal*, Vol. 16, No. 4, 1978, pp. 393–402.

[37] Gordnier, R. E., and Visbal, M. R., "Numerical Simulation of Delta-Wing Roll," AIAA Paper 93-0554, Jan. 1993.

[38] Pulliam, T. H., and Chaussee, D. S., "A Diagonal Form of an Implicit Approximate-Factorization Algorithm," *Journal of Computational Physics*, Vol. 39, No. 2, 1981, pp. 347–363.

[39] Lele, S. A., "Compact Finite Difference Schemes with Spectral-Like Resolution," *Journal of Computational Physics*, Vol. 103, No. 1, 1992, pp. 16–42.

[40] Gaitonde, D., Shang, J. S., and Young, J. L., "Practical Aspects of High-Order Accurate Finite-Volume Schemes for Electromagnetics," AIAA Paper 97-0363, Jan. 1997.

[41] Visbal, M. R., and Gaitonde, D. V., "High-Order-Accurate Methods for Complex Unsteady Subsonic Flows," *AIAA Journal*, Vol. 37, No. 10, 1999, pp. 1231–1239.

[42] Gaitonde, D., and Visbal, M. R., "High-Order Schemes for Navier–Stokes Equations: Algorithm and Implementation into FDL3DI," Air Force Research Lab., Technical Rept. AFRL-VA-WP-TR-1998-3060, Wright–Patterson AFB, OH, Aug. 1998.

[43] Gordnier, R. E., and Visbal, M. R., "Numerical Simulation of Delta-Wing Roll," *Aerospace Science and Technology*, Vol. 2, No. 6, 1998, pp. 347–357.

[44] Gordnier, R. E., "Computation of Delta-Wing Roll Maneuvers," *Journal of Aircraft*, Vol. 32, No. 3, 1995, pp. 486–492.

[45] Visbal, M. R., "Computational Study of Vortex Breakdown on a Pitching Delta Wing," AIAA Paper 93-2974, July 1993.

[46] Visbal, M., Gaitonde, D., and Gogineni, S., "Direct Numerical Simulation of a Forced Transitional Plane Wall Jet," AIAA Paper 98-2643, June 1998.

[47] Rizzetta, D. P., Visbal, M. R., and Stanek, M. J., "Numerical Investigation of Synthetic-Jet Flowfields," *AIAA Journal*, Vol. 37, No. 8, 1999, pp. 919–927.

[48] Rizzetta, D. P., Visbal, M. R., and Blaisdell, G. A., "A Time-Implicit High-Order Compact Differencing and Filtering Scheme for Large-Eddy Simulation," *International Journal for Numerical Methods in Fluids*, Vol. 42, No. 6, 2003, pp. 665–693.

[49] Rizzetta, D. P., and Visbal, M. R., "Application of Large-Eddy Simulation to Supersonic Compression Ramps," *AIAA Journal*, Vol. 40, No. 8, 2002, pp. 1574–1581.

[50] Rizzetta, D. P., Visbal, M. R., and Gaitonde, D. V., "Large-Eddy Simulation of Supersonic Compression-Ramp Flow by a High-Order Method," *AIAA Journal*, Vol. 39, No. 12, 2001, pp. 2283–2292.

[51] Rizzetta, D. P., and Visbal, M. R., "Large-Eddy Simulation of Supersonic Cavity Flowfields Including Flow Control," *AIAA Journal*, Vol. 41, No. 8, 2003, pp. 1452–1462.

[52] Steinbrenner, J. P., Chawner, J. P., and Fouts, C. L., "The GRIDGEN 3D Multiple Block Grid Generation System, Volume II: User's Manual," Wright Research and Development Center, Technical Rept. WRDC-TR-90-3022, Wright–Patterson AFB, OH, Feb. 1991.

K. Fujii
Associate Editor